Marine and Petroleum Geology 62 (2015) 28–43

Contents lists available at ScienceDirect

Marine and Petroleum Geology

journal homepage: www.elsevier.com/locate/marpetgeo

Pore characterization of organic-rich Lower Cambrian shales in Qiannan Depression of Guizhou Province, Southwestern China

Hui Tian [a, b], Lei Pan [a], Tongwei Zhang [b], Xianming Xiao [a, *], Zhaoping Meng [c], Baojia Huang [d]

[a] State Key Laboratory of Organic Geochemistry, Guangzhou Institute of Geochemistry, Chinese Academy of Sciences, Guangzhou 510640, China
[b] Bureau of Economic Geology, The University of Texas at Austin, United States
[c] College of Geoscience and Surveying Engineering, China University of Mining & Technology, Beijing 100083, China
[d] CNOOC Ltd, Zhanjiang 524057, China

ARTICLE INFO

Article history:
Received 29 August 2014
Received in revised form
6 January 2015
Accepted 13 January 2015
Available online 22 January 2015

Keywords:
Shale gas
Pore structure
Modified BET equation
DR equation
t-plot method

ABSTRACT

Nine organic-rich shale samples of Lower Cambrian black shales were collected from a recently drilled well in the Qiannan Depression, Guizhou Province where they are widely distributed with shallower burial depth than in Sichuan Basin, and their geochemistry and pore characterization were investigated. The results show that the Lower Cambrian shales in Qiannan Depression are organic rich with TOC content ranging from 2.81% to 12.9%, thermally overmature with equivalent vitrinite reflectance values in the range of 2.92–3.25%, and clay contents are high and range from 32.4% to 53.2%. The samples have a total helium porosity ranging from 2.46% to 4.13% and total surface area in the range of 9.08–37.19 m^2/g. The estimated porosity in organic matters (defined as the ratio of organic pores to the volume of total organic matters) based on the plot of TOC vs helium porosity is about 10% for the Lower Cambrian shales in Qiannan Depression and is far lower than that of the Lower Silurian shales (36%) in and around Sichan Basin. This indicates that either the organic pores in the Lower Cambrian shale samples have been more severely compacted than or they did not develop organic pores as abundantly as the Lower Silurian shales. Our studies also reveal that the micropore volumes determined by Dubinin–Radushkevich (DR) equation is usually overestimated and this overestimation is closely related to the non-micropore surface area of shales (i.e. the surface area of meso- and macro-pores). However, the modified BET equation can remove this overestimation and be conveniently used to evaluate the micropore volumes/surface area and the non-micropore surface areas of micropore-rich shales.

1. Introduction

Shales have received renewed attention in recent years because of their emergence as commercial hydrocarbon reservoirs in North America (Curtis, 2002; Montgomery et al., 2005; Jarvie et al., 2007; Pollastro, 2007). Shale gas evaluation and exploration in China, however, are still in its infancy and mainly focused around South China where the black marine shales were widely developed during Late Ediacaran (Doushantuo shale of Upper Sinian), Early Cambrian (Niutitang/Qiongzhusi shale of Lower Cambrian) and Early Silurian (Longmaxi shale of Lower Silurian) periods (Zou et al., 2010; Chen et al., 2011; Sun et al., 2012; Tan et al., 2014). These black shales are believed to have sourced the conventional petroleum system in and around Sichuan Basin (Zou et al., 2010), and the well-known Kaili-Majiang paleo-oil pools in Cambrian–Ordovician reservoirs in Guizhou province are also considered to be related to one or two of these shales (He et al., 2012, 2013). At the same time, the observation of abundant pyrobitumen in both the Lower Silurian and Lower Cambrian black shales reveals that part of liquid oils were retained after their primary migration and further cracked to gaseous hydrocarbons in following deep burial. These oil cracking gases, along with the gases from the cracking of residual kerogen, are the main source of shale gas (Jarvie et al., 2007; Hill et al., 2007; Strąpoć et al., 2010; Xia et al., 2013) and therefore both the Lower Cambrian and the Lower Silurian shales have promising potentials of shale gas (Wang et al., 2009; Zou et al., 2010; Long et al., 2012).

* Corresponding author. Postal address: 511#, Kehua Road, Tianhe District, Guangzhou City, Guangdong Province, 510640, China. Tel.: +86 2085290176; fax: +86 2085290706.
E-mail address: xmxiao@gig.ac.cn (X. Xiao).

http://dx.doi.org/10.1016/j.marpetgeo.2015.01.004
0264-8172/

Compared with the Lower Silurian shales, the Lower Cambrian shales are still less studied with respect to their potential as shale reservoirs, though they are more widely and stably distributed than the Lower Silurian shales throughout the whole Yangtz platform, and contain higher average TOCs and have greater thermal maturity levels (Wang et al., 2009; Han et al., 2013; Wang et al., 2014). Modica and Lapierre (2012) illustrated that the organic pores in gas shale seem to be related to thermal maturity (e.g., hydrocarbon generation), but the thermal maturity alone cannot controlled the porosity in gas shales when it reaches a very high levels (e.g. late gas generation stage with Ro larger than 2.0%, Curtis et al., 2012a). Therefore the investigation on the pore characterization of such old and high maturity Lower Cambrian shales can provide useful data for the evaluation of shale gas resources in China.

Unlike the conventional reservoirs of sandstones and carbonates that are characterized with micrometer scale pores, the shale reservoirs are usually dominated by nanometer-scale pores (Nelson, 2009). The identification of porosity and pore size distribution in gas shales has become a high research priority as they are key parameters for the commercial evaluation of a potential shale (Ross and Bustin, 2008, 2009; Loucks et al., 2009; Chalmers et al., 2012a, b; Clarkson et al., 2012a, b, c; Mastalerz et al., 2012, 2013; Milliken et al., 2013; Tian et al., 2013; Furman et al., 2014). The pore size terminology of the International Union of Pure and Applied Chemistry was recommended for the geoscientists working on shales, with micropores having widths less than 2 nm, mesopores between 2 and 50 nm, and macropores greater than 50 nm (Chalmers et al., 2009). To elucidate the complex pore systems of shales, researchers have utilized several measurement techniques to characterize the porosity, specific surface area and pore size distribution. While the field emission scanning electron microscopy/transmission electron microscopy (FE-SEM/TEM) and focused ion beam scanning electron microscopy (FIB-SEM) have been successfully used to directly identify pore types, shapes and sizes (Loucks et al., 2009; Bernard et al., 2012; Charlmers et al., 2012a; Milliken et al., 2013), the total porosity of shale is typically calculated by the difference between grain density and bulk density measured by He pycnometry and Hg immersion, respectively (Chalmers et al., 2012a) and the surface area and pore size distribution are mainly obtained by low pressure N_2/CO_2 gas adsorption and mercury injection capillary pressure (MICP) using various models (Ross and Bustin, 2009; Chalmers et al., 2012a, b; Mastalerz et al., 2012; Kuila and Prasad, 2013; Schmitt et al., 2013). The BET equation has been widely used to obtain the total surface area of shales, though it was originally designed for meso- and macroporous materials (Barrett et al., 1951) and strictly speaking, it is not applicable to micropore-rich materials, which leads to the appearance of the modified BET equation that incorporates the micropore volume as an unknown variable in the conventional BET equation, thus providing both micropore volume and non-micropore surface area (surface area contributed only by meso- and macro-pores) (Remy and Poncelet, 1995; Schneider, 1995; Marcilla et al., 2009). The micropore volume and surface area of shale can also be obtained using DR equation and t-plot method (Ross and Bustin, 2009; Mastalerz et al., 2012; Kuila and Prasad, 2013). However these methods have not been as well addressed for shales as for synthetic materials (Sousa-Aguiar et al., 1998; Scherdel et al., 2010). Since the shale gas can be stored as adsorbed gas (Curtis, 2002; Zhang et al., 2012) and the adsorption of methane in micropores is so different from that in meso- and macro-pores (Mosher et al., 2013), it is necessary to compare how different models evaluate differently the micropores in shales. In this study, we will (1) investigate the geochemistry and pore characterization of Lower Cambrian shales in southern Guizhou Province that could be used to compare with other black shales in South China and other basins in the world and (2) discuss how well the modified BET equation, DR equation and t-plot methods correlate with each other in determining the micropore volume of shales.

2. Geological settings

The Qiannan Depression is located in the southern part of Guizhou Province and bounded by three boundary faults to form a triangle shape (Fig. 1a). It is surrounded by the Qianzhong Uplift and the Wuling Depression in the north, the Xufengshang Uplift and the Guizhong Depression in the east and southeast and the Qianxinan Depression and the Luodian Faulted Depression in the west and southwest (He et al., 2012). The Qiannan Depression is subdivided into five secondary structural units (Fig. 1b), including Anshun Sag, Huangping Sag, Changshun Sag, Guiding Terrace and Dushan nose-shaped Low Uplift (He et al., 2012).

Previous studies illustrate that the Qiannan Depression today is a residual depression and has experienced complex tectonic evolutions (Xu et al., 2010; Wu et al., 2012). The Qiannan depression has double-layered basements, i.e., the deeper Proterozoic crystal basement and the shallower epimetamorphic Lower Neoproterozoic fold basement (Wu et al., 2012). After the Grenvile Orogen, the Qiannan Depression evolved to be part of passive continental margin until the late Caledonian Orogen that not only caused the appearance of Xufengshan Uplift in the east but also uplifted the Qiannan Depression and transformed it into foreland basin with transitional marine and terrestrial sediments during the late Silurian to early Devonian (Xu et al., 2010). As a response to the rapid marine transgression in early Cambrian, a set of black silicious rocks and carbonaceous shales were formed in deep-water shelf to basin facies, which lay over the Dengying dolomites deposited in the shallow water carbonate platform during late Neoproterozoic (Fig. 2, Mei et al., 2006). While this set of black shales is named as Niutitang formation in Guizhou Province and Qiongzhusi formation in and around Sichuan Basin, it is also named as the Jiumenchong formation in Qiannan Depression (Zeng, 2012). With the marine transgression of Paleo-Tethys Ocean, the Qiannan Depression rifted and subsided again to form the passive continental margin during the Hercynian cycle and continued until the Indosinian Orogen that caused the westward regression of Paleo-Tethys Ocean and formed again a foreland basin mainly filled by transitional to terrestrial sediments during Indosinian cycle. During Yanshanian cycle the westward tectonic compression of Xufengshan Uplift transformed the Qiannan Depression into an inland basin that was further deformed by the following Himalaya Orogeny, leading to the extensive erosion of Paleozoic to Mesozoic sediments (He et al., 2012; Wu et al., 2012).

3. Samples and experiments

3.1. Samples

Nine core samples were collected from a recently drilled well that was designed for the evaluation of the Lower Cambrian in Huangping Sag, Qiannan Depression (Fig. 1b) and the black shales were sampled in the interval of 2371–2415 m (Table 1).

3.2. Organic geochemistry, petrology and helium porosity

The total organic carbon (TOC) was measured by LECO CS-200 analyzer after the samples were treated by hydrochloric acid to remove the carbonates.

The maceral observation was performed on one-side polished blocks with a Leica MPV microscope using reflected white and

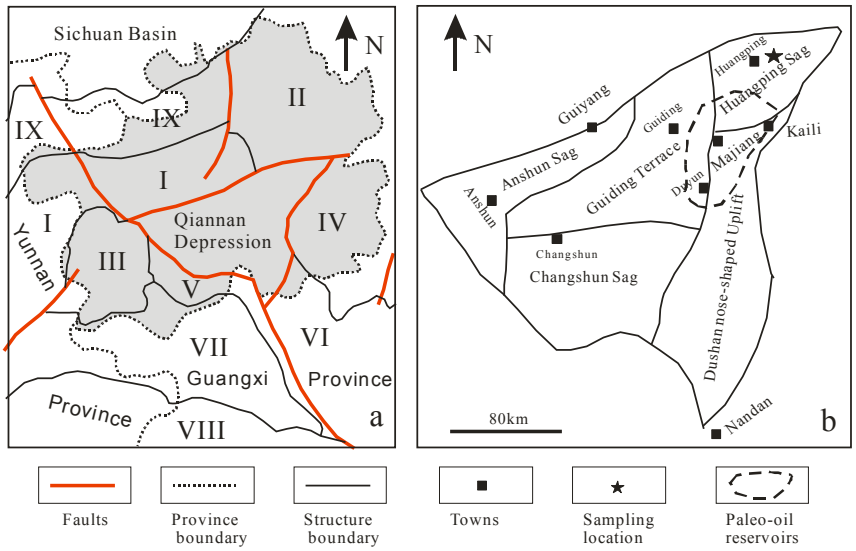

Figure 1. Skematic maps showing the location of Qiannan Depression (a) and its structural units and sampling location (b) (Modified from He et al., 2012; Hou et al., 2012). I: Diandong–Qianzhong Uplift; II: Wuling Depression; III: Qianxinan Depression; IV: Xufengshan Uplift; V: Luodian Faulted Depression; VI: Guizhong Depression; VII: Nanpanjiang Depression; VIII: Maguan Uplift; IX: Dian-Qian North Depression.

fluorescent light, and the identification of macerals in shales was referred to Stach et al. (1982) and Taylor et al. (1998). Due to the lack of vitrinite in the sampled shales, the reflectance of pyrobitumen was measured on polished blocks using a 3Y microphotometric system. The random reflectance was measured in oil immersion (n = 1.518) at 546 nm using a 50×/0.85 objective lens. The pyrobitumen reflectance (BRr) was then converted to equivalent vitrinite reflectance (VRr) using the equation of Schoenherr et al. (2007), i.e., VRr = (BRr + 0.2443)/1.0495.

X-ray diffraction (XRD) analysis of shale powders was carried out on a Bruker D8 Advance X-ray diffractometers at 40 kV and 30 mA with a Cu Kα radiation (λ = 1.5406 for CuKα1). Stepwise scanning measurements were performed at a rate of 4°/min in the range of 3°–85° (2θ). The relative mineral percentages were estimated semi-quantitatively using the area under the curve for the major peaks of each mineral with correction for Lorentz Polarization (Chalmers and Bustin, 2008).

The helium porosity of shales was determined by bulk density coupled with skeletal density (Chalmers et al., 2012a). Samples (40–50 g) crushed between 20 and 40 mesh sizes (830 and 380 μm) and dried at 110 °C overnight were used in determining the skeletal density by helium pycnometry at a pressure of less than 25 psia. For the measurement of bulk density, the samples were weighted in air before and after coated by paraffin of known density, then the paraffin coated samples were weighted both in the air and in the water of known density to obtain the sample's bulk volume, finally the bulk density was calculated by the weight in air and the bulk volume (Tian et al., 2013).

3.3. Low pressure N_2 and CO_2 adsorption

The N_2 and CO_2 adsorptions were carried out on Micromeritics ASAP 2020^M apparatus. The shale samples were crushed into grains about 60–100 mesh size (250–150 μm), dried in vacuum oven at 110 °C overnight and degassed under high vacuum (<10 mmHg) for 12 h at 110 °C in the apparatus to further remove adsorbed moisture and volatile matter. For nitrogen adsorption, the sample was kept at the temperature of liquid nitrogen temperature (77.35 K at 101.3 kPa). For CO_2 adsorption, the temperature of the sample was 273 K (0 °C). The relative pressure (p/p_0) for N_2 and CO_2 adsorption ranges from 0.009 to 0.995 and 0.00001 to 0.032, respectively. Both adsorption and desorption isotherms were measured to investigate the hysteresis types for the N_2 adsorption.

3.4. FE-SEM observation

The FE-SEM imaging of nanopores was performed using the Hitachi S8010 systems on the surfaces prepared by Ar ion milling (IM4000, Hitachi High-Tech) with an accelerating voltage of 3 kV and a milling time of 4–8 h. The Su 8010 system incorporates semi-inlens electron optics with the Super-ExB filter and an Upper detector above the objective lens. By simple shifting of a slider with the mouse on the user interface, the voltage of the Super ExB filtering & conversion electrode is changed, allowing for a free adjustment of the SE-BSE signal ratio from a pure SE image. Thus both secondary electron (SE) and backscattered electron (BSE) can be acquired simultaneously through the Upper detector. These images provided important qualitative information on general locations of pores throughout the sample (Loucks et al., 2009). Lower accelerating voltages (1–2 kV) with working distances of about 1.5–4 mm were typically used on these systems to prevent beam damage to the samples.

3.5. Conventional and modified BET equation

The BET equation was originally designed to assess the surface areas of nonporous or meso-macrous porous materials and presented in the following form (Eq. (1)),

$$\frac{V_{ads}}{V_m} = \frac{C_{BET} \cdot p/p_0}{(1 - p/p_0) \cdot [1 + (C_{BET} - 1) \cdot p/p_0]} \quad (1)$$

where p/p_0 represents the relative pressure, V_{ads} denotes the adsorbed volume at equilibrium pressure p, V_m is the monolayer volume and the constant C_{BET} reflects the net heat of adsorption, i.e. the difference in adsorption heats between the first layer and other layers.

Then surface area (S_{BET}) with unit of m^2/g was calculated using the following equation:

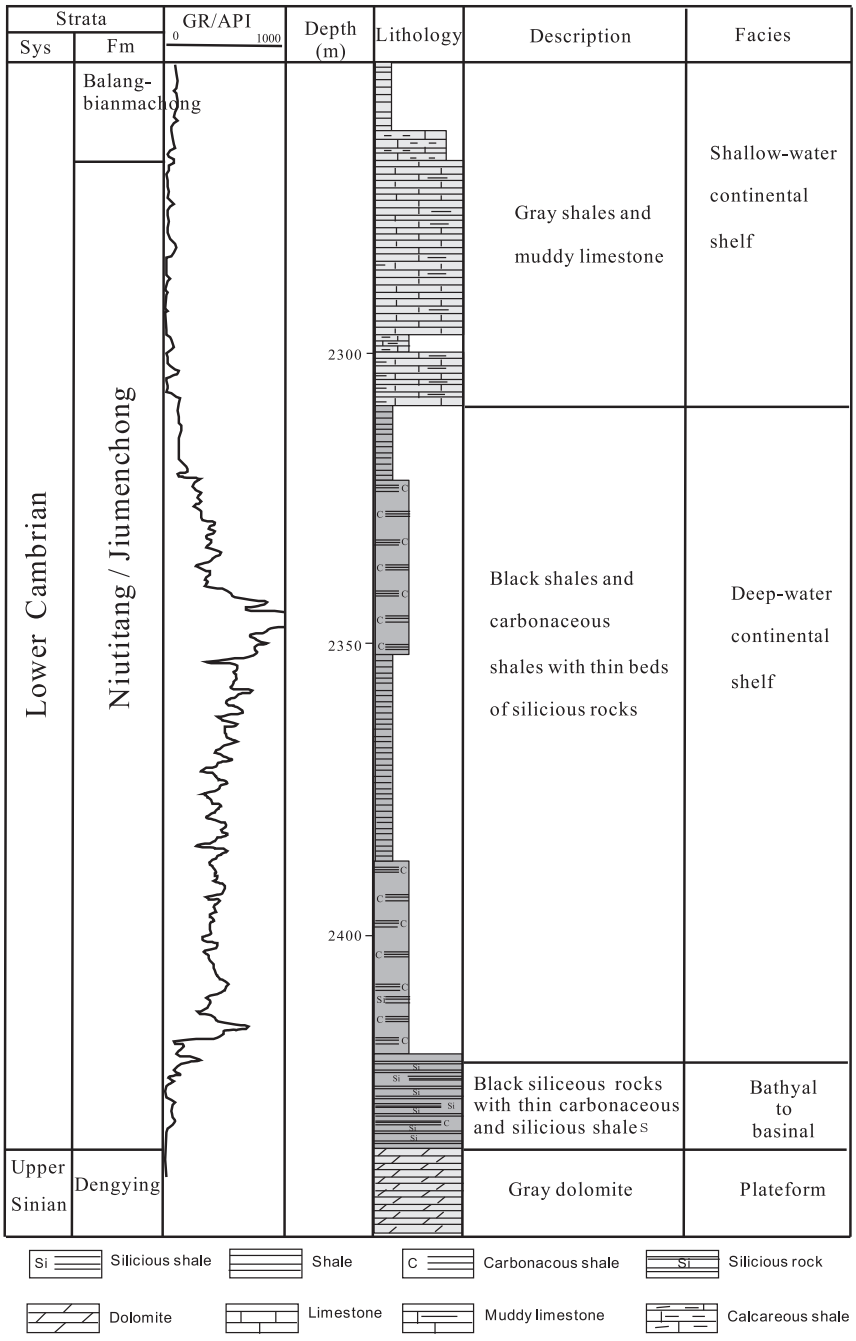

Figure 2. Stratigraphical column showing the black shales in the Lower Cambrian strata and their depositional environments (modified from Hou et al., 2012; Wu et al., 2012).

$$S_{BET} = \frac{0.001 \times V_m}{22.4} \times N \times A_{N_2} \tag{2}$$

with V_m the monolayer volume in cm^3/g; N the Avogadro' number; A_{N_2} the atomic surface area of N_2 (0.162 nm^2 at 77 K, Sing et al., 1985).

To avoid the complicated mathematical fitting, the original BET equation is also rewritten in its linear form (Eq. (3)), thus the V_m and C_{BET} can be respectively calculated from the slope and the intercept of the regressed line in the plot of p/p_0 vs $\frac{p/p_0}{V_{ads}\cdot(1-p/p_0)}$.

$$\frac{p/p_0}{V_{ads}\cdot(1-p/p_0)} = \frac{1}{V_m\cdot C_{BET}} + \frac{C_{BET}-1}{V_m\cdot C_{BET}}\cdot\frac{p}{p_0} \tag{3}$$

To reduce any subjectivity in the selection of fitting range of the BET plot and give an objective way of determining the fitting range of the BET plot rather than using the same relative pressure range for all materials, Rouquerol et al. (2007) suggested some criteria for the selection of relative pressure range, including (1) the resulting parameter C_{BET} is positive; (2) the intercept on the ordinate of the BET-plot is positive and (3) the term $V_{ads}(p_0 - p)$ should continuously increase with p/p_0, if not, the pressure rang should be narrowed. The third rule is based on another linear form of original BET equation that requires a positive relationship between $V_{ads}(p_0 - p)$ and p (Eq. (4)).

$$\frac{p_0}{V_{ads}\cdot(p_0-p)} = \frac{1}{V_m\cdot C_{BET}}\cdot\frac{p_0}{p} + \frac{C_{BET}-1}{V_m\cdot C_{BET}} \tag{4}$$

Table 1
The TOC, pyrobitumen reflectance and mineral composition.

Sample	[a]Age	Lithology	Depth (m)	TOC (%)	[b]Mean pyrobitumen reflectance (%)	Bulk density (cm^3/g)	Helium grain density (cm^3/g)	Helium porosity (%)	Mineral composition (%)				
									Quartz	Feldspar	Carbonate	Pyrite	Clays
HY1	ϵ_1	Black shale	2371.03	12.90	3.06 (45)	2.3396	2.4380	4.04	39.4	11.0	[c]nd	2.7	46.8
HY2	ϵ_1	Black shale	2373.60	9.65	3.01 (40)	2.3208	2.4208	4.13	29.7	10.5	4.3	2.3	53.2
HY3	ϵ_1	Black shale	2380.02	5.68	3.10 (38)	2.4484	2.5194	2.82	31	11.8	6.2	4.2	46.8
HY4	ϵ_1	Black shale	2384.62	6.14	2.82 (36)	2.4561	2.5297	2.91	35.1	16.5	5.0	4.3	39.1
HY5	ϵ_1	Black shale	2389.75	2.81	2.82 (38)	2.5200	2.5836	2.46	31.3	18.8	13.3	4.2	32.4
HY6	ϵ_1	Black shale	2396.12	4.32	3.02 (42)	2.4265	2.5257	3.93	41.6	17.7	nd	3.8	36.8
HY7	ϵ_1	Black shale	2401.45	6.92	3.17 (36)	2.4448	2.5116	2.66	35.7	14.6	3.4	2.8	43.5
HY8	ϵ_1	Black shale	2407.17	6.87	nd	2.4005	2.4869	3.47	34.5	17.1	4.9	2.4	41.1
HY9	ϵ_1	Black shale	2415.14	5.89	3.04 (45)	2.4932	2.5574	2.51	23.2	18.8	nd	5.5	52.4

[a] ϵ_1: Lower Cambrian.
[b] The figures in bracket indicate numbers of individual measurements.
[c] nd: no data.

As mentioned earlier (Rouquerol et al., 2007), the BET equation was not originally designed for micropores. To characterize the surface areas of microporous–mesoporous solids like shales, the conventional BET equation could be modified as follow (Eq. (5), Schneider, 1995):

$$V_{ads} = \frac{V_m \cdot C_{BET}^{ext} \cdot p/p_0}{(1 - p/p_0) \cdot \left[1 + \left(C_{BET}^{ext} - 1\right) \cdot p/p_0\right]} + V_{mic} \quad (5)$$

where V_{mic} represents the net volume of adsorbate which fills the micropores. The C_{BET}^{ext} means the BET C value that is not affected by micropores. Then the three unknown parameters in Eq. (5) were fitted by any non-linear fitting procedure with the sum of squared deviations between experimental and calculated adsorption amounts used as the objective function in the relative pressure range of 0.05–0.35 (Schneider, 1995; Šolcová et al., 2009).

3.6. Dubinin–Radushkevich equation and t-plot method

Different from the BET equation that describes the multilayer adsorption of gas in meso- and macro-pores, the Dubinin–Radushkevich (DR) equation (Eq. (6)) describes the filling of gas in micropores and the intercept of the plot of $\log(V_{ads})$ vs $\log(p/p_0)$ yields the micropore volume (Sing et al., 1985).

$$\log(V_{ads}) = \log(V_{mic}) - 2.303 \cdot (RT/\beta E_0)^2 \cdot \log^2(p/p_0) \quad (6)$$

where V_{ads} is the volume of sorbed gas at equilibrium pressure, V_{mic} is the total micropore volume, R is the gas constant, T is the Kelvins temperature, β is the affinity coefficient and taken as 0.46 and 0.34 for CO_2 and N_2 at 273 K and 77 K, respectively and (Carrasco-Marín et al., 1996), p is equilibrium pressure and p_0 is saturation vapor pressure.

The micropore volume was also estimated using the t-plot method based on N_2 adsorption (de Boer et al., 1966; Hodson, 1999;

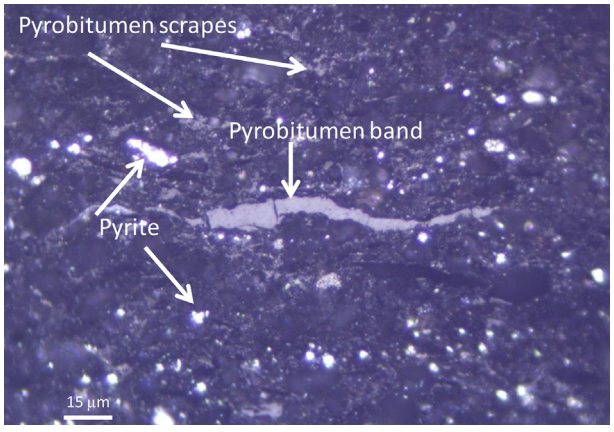

Figure 3. Typical microphotograph of whole rock, showing the pyrobitumen and pyrite. The brightest is the pyrite crystals and/or framboid pyrites. The pyrobitumen is gray and occurs in shapes of both bands and scrapes.

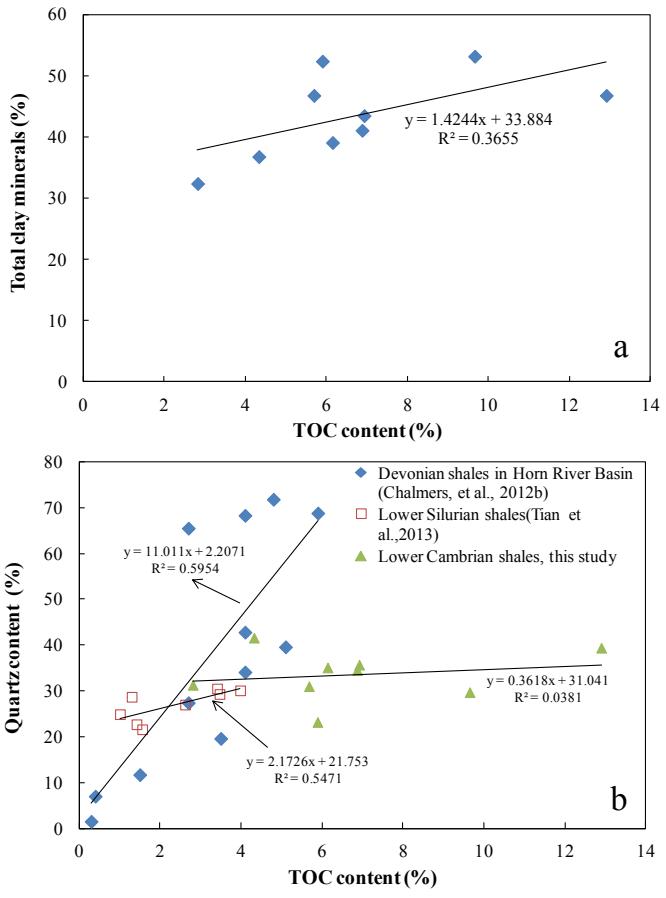

Figure 4. Plots showing the relationships of TOC content with total clays content (a) and quartz content (b). The weakly positive relationship indicates the quartz of biogenic origin is minor for our samples.

Scherdel et al., 2010). In t-plots, the adsorbed N_2 volume (V_{ads}) is plotted against the statistical thickness (t) of the adsorbed layer of N_2 adsorption. If the plot yields a straight line that passes through the origin, then the sample is considered to be free of micropores (de Boer et al., 1966). On the contrary, the t-plot of the material containing micropores shows a straight line at medium t values and a concave–down curve at lower t values. At higher t values, convex-up deviation from the linear trend indicates capillary condensation in mesopores. Thus the slope (t) and intercept (b) of the regressed straight line gives the non-micropore surface area (S_{ext}) and the micropore volume (V_{mic}), respectively (de Boer et al., 1966). When the V_{ads} is in unit of cm^3/g and t is in unit of angstrom, S_{ext} in unit of m^2/g is given by:

$$S_{ext} = 15.47 \times k \tag{7}$$

and V_{mic} in cm^3/g is given by

$$V_{mic} = 0.001547 \times b \tag{8}$$

Thus the surface area of micropores (S_{mic}) can be estimated by subtracting the non-micropore surface area (S_{ext}) calculated by the t-plot method from the total surface area (S_{BET}) obtained by the conventional BET equation (Hodson, 1999; Rouquerol et al., 2007; Scherdel et al., 2010; Kuila and Prasad, 2013).

The most frequently used 'universal thickness curve' is based on the Harkins–Jura model for N_2 adsorption (de Boer et al., 1966):

$$t = \left[\frac{13.99}{0.034 - \log(p/p_0)}\right]^{1/2} \tag{9}$$

Considering the shale samples contain organic matter, the Carbon Black model (Magee, 1995) was also used to calculate the statistical thickness (t):

$$t = 0.88 \times (p/p_0)^2 + 6.45 \times (p/p_0) + 2.98 \tag{10}$$

Where, p/p_0 is the relative pressure and the unit of t is angstrom.

It is worthy to note that the analyzed samples have to have the same chemical composition and surface characters as those from which the above two thickness models were obtained. However it is not always possible to know whether or not they are the same. Therefore some authors suggested that the thickness models (Eq. (11)) should be specifically obtained from the BET isotherm parameter C (Lecloux and Pirard, 1979):

$$t = t_0 \frac{k \cdot x}{1 - k \cdot x} \times \frac{1 - (m+1) \cdot (kx)^m + m \cdot (kx)^{m+1}}{\frac{1}{C_{BET}^{ext}} + \frac{C_{BET}^{ext} - 1}{C_{BET}^{ext}} \cdot k \cdot x - (kx)^{m+1}} \tag{11}$$

With the nitrogen monolayer film thickness t_0 = 3.54 Å and adjustable parameters k = 0.95 and m = 4.18. The parameter C_{BET}^{ext} has the same meaning as in the modified BET equation (Eq. (5)) and x is the relative pressure p/p_0.

3.7. Barrett–Joyner–Halenda (BJH) model and pore size distribution

The pore size distribution was calculated using the BJH model that describes the capillary condensation phenomenon in a cylindrical pore (Barrett et al., 1951). It is assumed that the condensation of N_2 in a pore of radius r takes place in the 'core' region, i.e., the inner part of the pore that is calculated by subtracting the statistical thickness (t) from the pore radius r. Using this model, it is predicted that the condensation of nitrogen in a pore of radius r occurs at a pressure given by the following modified Kelvin equation:

$$\ln(p/p_o) = -\frac{\alpha \gamma_N V_1}{RT(r-t)} \tag{12}$$

Where, p/p_0 is the relative pressure, γ_N and V_1 are the surface tension and molar volume of liquid nitrogen, respectively; R is the gas constant, T is the temperature at which the isotherm is measured and α is a factor that accounts for the shape of the gas/liquid interface. During the adsorption process, the shape is assumed to be cylindrical and the value of α is 1 (Coasne et al.,

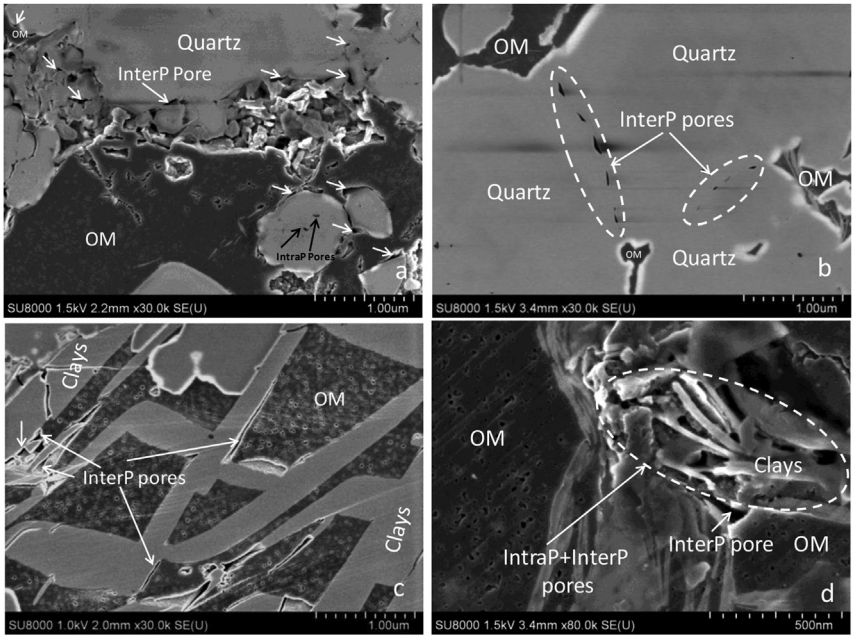

Figure 5. Field emission scanning electron microscope (FE-SEM) images showing interP and intraP pores. OM = organic matter; InterP = inter-particle; IntraP = intra-particle pores. a: sample HY2; b: sample HY8; c: sample HY1; d: sample HY9.

2004). The statistical thickness (t) was calculated by the Harkins–Jura model for N_2 adsorption (de Boer et al., 1966).

4. Results and discussions

4.1. Organic geochemistry and petrology

The total organic carbon contents (TOC) for the nine shale samples range from 2.81% to 12.90% (Table 1). The organic fraction is dominated by maceral assemblages of micrinite, interpreted as the residual organic matter after oil generation and expulsion (Stach et al., 1982; Ross and Bustin, 2009), and pyrobitumen formed by the cracking of retained oil in shales (Fig. 3; Pepper and Dodd, 1995; Bernard et al., 2012; Mahlstedt and Horsfield, 2012). The measured pyrobitumen reflectance values range between 2.82% and 3.17% (Table 1) and the calculated equivalent vitrinite reflectances using the equation of Schoenherr et al. (2007) are in the range of 2.92–3.25%, within the stage of dry gas generation. Note that this transformation may bear some uncertainty due to the fact that different populations of pyrobitumen may have higher or lower reflectances compared to true vitrinite (Milliken et al., 2013). The mineralogical compositions of the nine black shale samples are listed in Table 1. All the samples are clay rich, ranging from 32.4% to 55.6%, and a weakly positive trend between TOC content and the total clay content was observed (Fig. 4a). The quartz contents

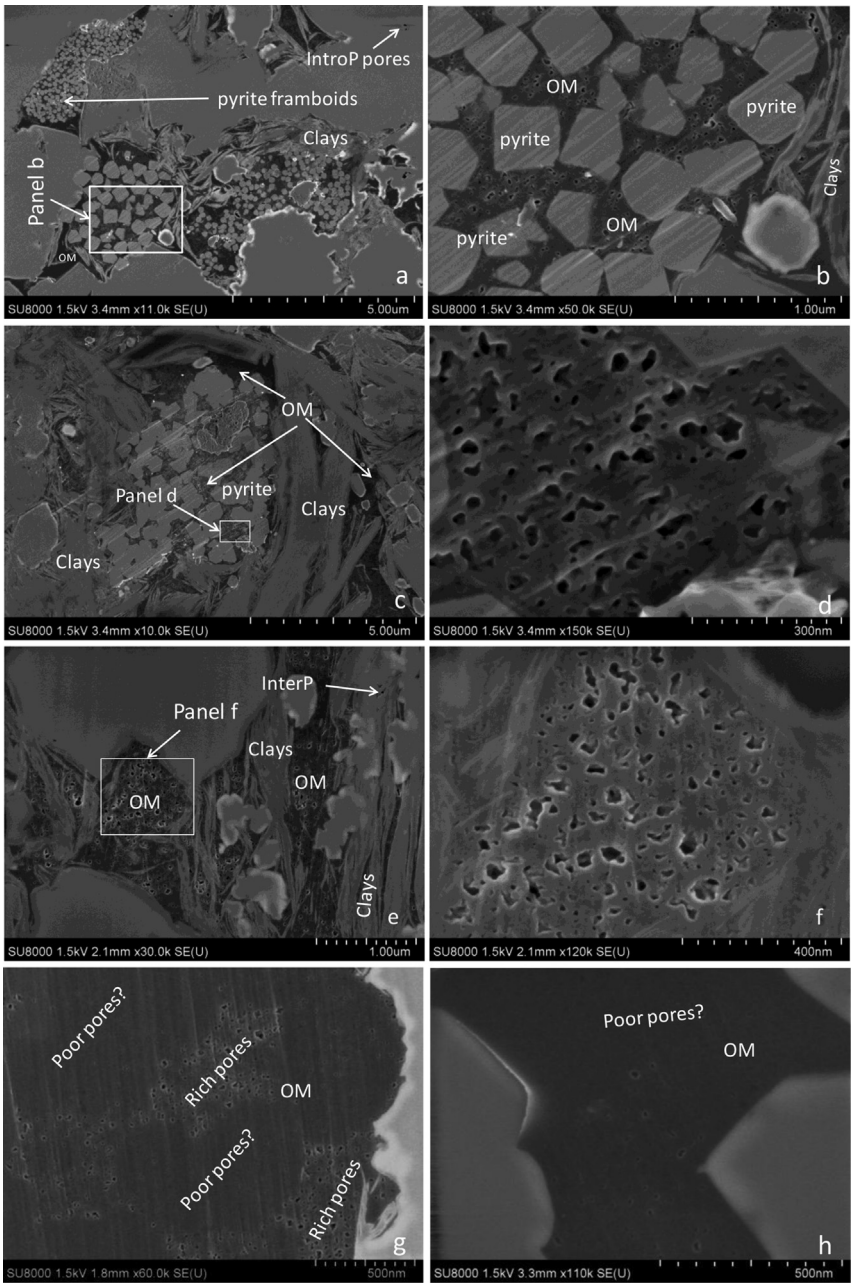

Figure 6. Field emission scanning electron microscope (FE-SEM) images showing pores in organic grains surrounded by pyrite framboids (a–d, sample HY 9) and clastic minerals (e and f, sample HY 7). The heterogeneity of organic pores is illustrated in g (sample HY 7) and h (sample HY 6). InterP = inter-particle; IntraP = intra-particle pores; OM = organic matter.

vary from 21.5% to 39.4% and show no obvious relationship with TOC, which is different from the positive correlation between TOC and quartz contents in Devonian gas shales in Horn River Basin, Canada and some Lower Silurian shales in South China (Fig. 4b). However, no positive correlation between TOC and quartz does not always indicate no biogenic quartz, and additional data, such as element data of SiO_2 and Zr and their correlation (Ratcliffe and Wright, 2012), should be obtained in the future to confirm whether or not the biogenic quartz is present in Lower Cambrian shale samples. The carbonate contents vary from below detection to 13.3%, whereas the feldspar content ranges from 10.0% to 18.8%.

4.2. FE-SEM observation and pore types

According to their occurrences, pores in shales can be grouped to inter-particle (interP) and intra-particle (intraP) pores (Chalmers et al., 2012a, b; Loucks et al., 2012). The interP pores in our samples are observed between grains that range from soft and ductile (e.g. clays) to hard and rigid (e.g. quartz) and have various shapes with pore size between tens to about one hundred nanometers (Fig. 5). Especially, the interP pores are commonly observed between the organic matters and clay minerals (Fig. 5c) and this is probably related to the shrinking of clay minerals and/or decompression effect after the retrieval from subsurface (Chalmers et al., 2012a). The IntraP pores are mainly indentified within organic matters and clay minerals. In clay aggregates, both IntraP and InterP pores can be developed together (Fig. 5d), which forms a complex pore structure. The most important intraP pores in our samples are organic pores that have cylinder, slit, elliptical and irregular shapes, and most of them have sizes of less than 50 nm (Fig. 6). The organic matters holding pores can occur within pyrite framboids (Fig. 6a, b, c, d) and between clastic minerals (Fig. 6e, f). Based on the present 2D images, theses organic-matter pores occur isolated or connected with each other. It is worthy to note that not all organic matter grains are the same porous. As illustrated in Figure 6g and h, the pores are heterogeneously developed in different parts of the same organic matter grain. The heterogeneity of organic pores was also been reported in some North American shales and was probably related to the change in the natures of organic matter grains (Curtis et al., 2012a,b; Loucks et al., 2012).

4.3. Helium porosity and relationship with TOC contents

The helium density (e.g. skeletal or grain density) of the nine samples ranges from 2.4208 g/cm^3 to 2.5836 g/cm^3 and their corresponding bulk density is in the range of 2.3208 g/cm^{3}to 2.5200 g/cm^3, which yields porosity ranging from 2.46% to 4.13% (Table 1) and these values are within the porosity range of the North American shales (Bruner and Smosna, 2011; Chalmers et al., 2012a,b; Hao and Zou, 2013). As revealed by the FE-SEM images, one distinct difference between the conventional and shale reservoirs lies in that the shale reservoirs host abundant organic pores in organic matters (Loucks et al., 2009). Except the sample HY6, a positively linear relationship between the total helium porosity and TOC was also observed with a regressed slope and intercept of 0.20 and 1.65, respectively (Fig. 7). By assuming that the density of organic matters is half of the shale density (Passey et al., 2010), the slope of 0.20 indicates the average porosity of organic matters is 10%. On the other hand, the intercept means the average inorganic porosity of our samples is 1.65% because there are no organic pores when the TOC is extrapolated to zero. Of course, the validity of this assumption and extrapolation depends on the size of dataset, and the larger

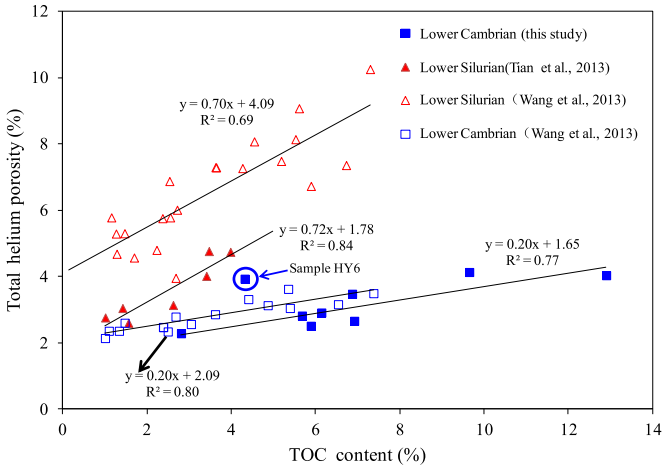

Figure 7. Relationships of TOC content with total porosity for the Lower Cambrian and Lower Silurian shales in Sichuan Basin and Qiannan Depression.

the dataset is, the more accurate the results are. For the sample HY6, its total helium porosity deviates above the regressed trend (Fig. 7) and this might be related to its highest content of quartz (Table 1), which could provide more intra-particle pores (Loucks et al., 2012).

Figure 7 also presents the relationships between total porosity and TOC content for the Lower Cambrian and Silurian shales in and around Sichuan Basin. Generally both the slope and intercept for the Lower Cambrian shales are similar, but smaller than those for the Lower Silurian shales whose porosity in organic matters is as high as about 36% (Tian et al., 2013), indicating that the organic matters in the Lower Silurian shales are more porous than the Lower Cambrian shales. Meanwhile the porosity of organic matters in the Lower Cambrian shales (about 10%) is also significantly lower than those in some shales in North America. For example, Sigal (2012) reported an organic porosity ranging from 29% to 31% in five Barnnet shales samples using NMR technology, and Modica and Lapierre (2012) proposed a model that predicts a maximum organic porosity of about 40% at Ro 1.6% for typical type II kerogen, and Curtis et al. (2012a) also observed an organic porosity of about 35% in a Woodford shale sample with Ro = 3.6%. The above data indicate that the higher maturity is not the only factor that leads to the decrease of organic porosity in the Lower Cambrian shales, and one possible reason might be that they have expelled more gases than the Lower Silurian shales, which leads to the more compaction of both organic and inorganic pores (Milliken et al., 2013). Therefore more work should be focused on the evolution history of organic pores in the future.

4.4. Isotherms of N_2 and CO_2 adsorption

The isotherms of adsorption and desorption of N_2 at liquid nitrogen temperature (77.35 K) are presented in Figure 8. The adsorption amount at p/p_o around 0.995 varies from 8.9 cm^3/g to 21.2 cm^3/g for different samples, and shows a positive relationship with TOC (Fig. 8j). All the isotherms show a hysteresis pattern but do not show a plateau at higher pressures, implying that the samples contain both mesopores and macropores (Sing et al., 1985). Meanwhile the large adsorption amount at low relative pressure ($p/p_o < 0.01$) indicates presence of micropores. The isotherms also show the 'forced closure' of the desorption branch at $p/p_o \approx 0.45$, which is referred to as the 'Tensile Strength Effect' and is a result of instability of the hemispherical meniscus during desorption in

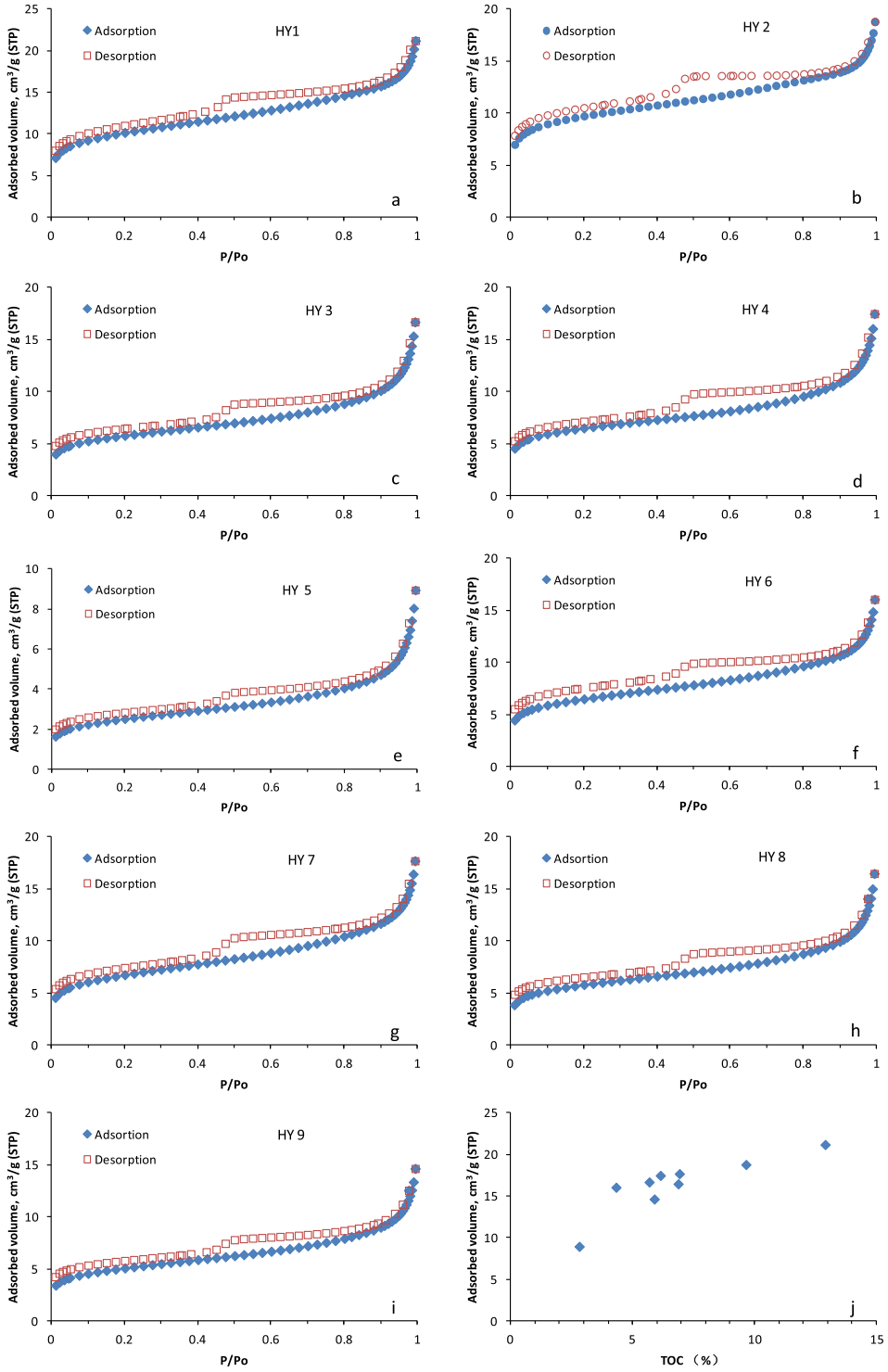

Figure 8. Nitrogen gas adsorption and desorption isotherms at 77 K (a–i) and the relationship of TOC content with the adsorption amount at $p/p_0 = 0.995$ (j).

pores with critical diameters approximately 4 nm (Groen et al., 2003). The curves of CO_2 adsorption at 273 K is presented in Figure 9 and the adsorbed amounts at maximum relative pressure range from 2.84 cm^3/g to 3.74 cm^3/g. Because the maximum equilibrium pressure in this study is about 1 bar and far lower than the CO_2 saturation pressure (34.5 bar) at 273 K, the maximum adsorption amount can not be directly used to represent the real micropore volume.

4.5. Specific surface area and micropore volume

The specific surface areas calculated from the nitrogen adsorption isotherms using the classic and modified BET equations and various t-plot models are presented in Table 2. To fully test the modified BET equation, some recalculations on the Lower Silurian shale samples (Tian et al., 2013) were also conducted and included in Table 2. As mentioned previously, the classic BET

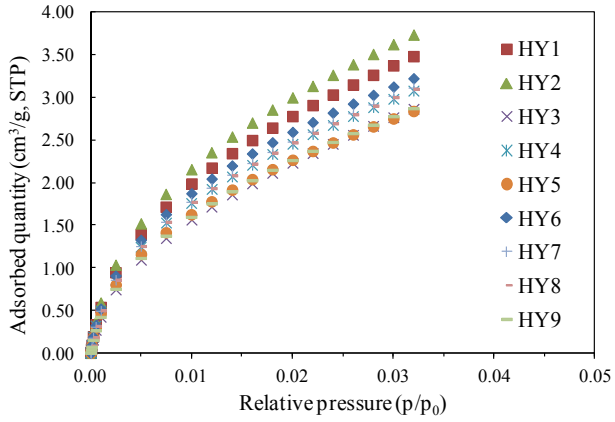

Figure 9. CO_2 gas adsorption isotherms at 273 K for the nine Lower Cambrian shale samples.

method provides the total specific surface area (S_{BET}) while the modified BET equation and t-plot method typically provides both the non-micropore specific surface area (S_{ext}) and the micropore volume. An example of modified BET equation is presented in Figure 10a. It is clear to see that the classic BET equation only applies to lower relative pressure and significantly overestimates the adsorption at relative pressure higher than 0.2. However the modified BET equation applies to relative pressure up to 0.4, and the covered range is typical of nonporous and or meso- and macro-porous materials, indicating that the modified BET equation can provide the non-micropore surface area and micropore volume of shales at the same time. The total specific surface area (S_{BET}) for the nine samples ranges from 9.08 m^2/g to 31.79 m^2/g and has a positive relationship with TOC (Fig. 10b). This relationship was also previously observed for many gas shales in North American basins (Chalmers and Bustin, 2008; Ross and Bustin, 2009). While the non-micropore surface area (S_{ext}) calculated by the modified BET equation ranges from 3.55 m^2/g to 12.41 m^2/g, the S_{ext} values calculated by the t-plot method are in the range of 4.01–13.77 m^2/g when the fitted C values in modified BET equation (Table 2) are used in the Lecloux and Pirard model (1979). At the same time, the S_{ext} values calculated by Harkins–Jura model (de Boer et al., 1966) and Carbon Black model (Magee, 1995) are in the range of 3.64–7.38 m^2/g and 4.43–14.45 m^2/g, respectively. Figure 11 compares the relationships of non-micropore surface area (S_{ext}) calculated by modified BET equation and various t-plot models, and reveals that the non-micropore surface areas (S_{ext}) by the modified BET equation and t-plot model of Lecloux and Pirard (1979) are most similar and linearly related (Fig. 11c), which further supports that both the BET method and the t-plot method are intrinsically identical when the micropore volume are deducted from the isotherms and the proper thickness model is used in the t-plot method.

Similar to the Devonian–Mississippian Muskwa and Besa River shales from northern British Columbia, western Canada (Ross and Bustin, 2009), the micropore surface areas (S_{mic}), obtained by subtracting the non-micropore surface area (S_{ext}) from the total surface area (S_{BET}) (Rouquerol et al., 2007), also show a positive correlation with TOC except a sample with highest TOC content (Fig. 12a). Note that the S_{ext} also show positive correlation with TOC content (Fig. 12b), indicating that the organic matters provide pores ranging from micropores to meso- and macropores, which has been proved by FE-SEM observations in our samples and other shales (Loucks et al., 2009; Chalmers et al., 2012a; Milliken et al., 2013).

Table 2
The total surface area (S_{BET}) calculated by classic BET equation, the non-micropore surface area (S_{ext}), micropore surface area (S_{mic}) and micropore volume (V_{mic}) calculated by various models.C_{BET}^{ext} means the BET C value that is not affected by micropores in the modified BET equation.

Samples	[a]Age	S_{BET} (m^2/g)	DR equation N_2 adsorption		DR equation CO_2 adsorption		Modified BET equation			t-plot models								
										Harkins–Jura model			Carbon black model			C-value based model[c]		
			V_{mic} ($cm^3/100g$)	S_{mic} (m^2/g)	V_{mic} ($cm^3/100g$)	S_{mic} (m^2/g)	V_{mic} ($cm^3/100g$)	C_{BET}^{ext}	S_{ext} (m^2/g)	S_{mic} (m^2/g)	V_{mic} ($cm^3/100g$)	S_{ext} (m^2/g)	S_{mic} (m^2/g)	V_{mic} ($cm^3/100g$)	S_{ext} (m^2/g)	V_{mic} ($cm^3/100g$)	S_{mic} (m^2/g)
HY1	ϵ_1	37.19	1.53	19.01	1.06	21.59	1.14	13.92	12.41	24.78	6.51	1.58	30.68	14.45	0.95	22.74	13.77	1.11	23.42
HY2	ϵ_1	35.85	1.47	18.78	1.15	23.60	1.14	14.36	10.26	25.59	4.26	1.59	31.59	11.38	1.02	24.48	10.80	1.14	25.05
HY3	ϵ_1	21.03	0.88	10.30	0.82	16.90	0.67	10.76	6.94	14.08	7.09	0.63	13.94	8.81	0.52	12.21	7.96	0.64	13.07
HY4	ϵ_1	23.78	0.99	11.85	0.89	19.00	0.77	10.79	7.08	16.70	7.38	0.71	16.40	8.51	0.64	15.27	7.88	0.76	15.90
HY5	ϵ_1	9.08	0.36	4.30	0.84	17.90	0.28	9.70	3.55	5.53	3.64	0.25	5.44	4.43	0.20	4.65	4.01	0.27	5.07
HY6	ϵ_1	23.58	0.99	11.64	1.02	20.74	0.74	10.70	7.97	15.60	5.46	0.93	18.11	9.55	0.60	14.02	9.02	0.72	14.56
HY7	ϵ_1	24.32	1.01	11.90	0.96	19.54	0.75	10.72	8.88	15.43	6.93	0.89	17.39	11.13	0.57	13.19	10.07	0.73	14.25
HY8	ϵ_1	20.99	0.90	9.70	0.95	19.44	0.66	10.92	7.26	13.73	6.59	0.67	14.40	8.76	0.52	12.23	8.17	0.64	12.81
HY9	ϵ_1	18.30	0.77	8.73	0.88	17.57	0.56	10.69	6.91	11.39	6.08	0.59	12.22	8.40	0.43	9.90	7.78	0.54	10.52
[b]PY1	S_1	*9.31*	0.37	4.62	0.37	8.47	0.27	13.47	3.90	5.42	*4.36*	*0.22*	*4.95*	*5.04*	*0.18*	*4.28*	4.21	0.26	5.10
[b]PY2	S_1	*5.06*	0.20	2.41	0.46	9.99	0.14	14.48	2.31	2.75	*3.01*	*0.09*	*2.05*	*3.13*	*0.08*	*1.93*	2.40	0.14	2.66
[b]PY3	S_1	*7.86*	0.32	11.87	0.42	9.38	0.22	14.18	3.44	4.42	3.97	*0.17*	*3.89*	*4.46*	*0.14*	*3.40*	3.72	0.21	4.14
[b]PY4	S_1	*6.11*	0.24	2.79	0.33	7.41	0.16	13.53	2.84	3.27	3.54	*0.11*	*2.57*	*3.66*	*0.10*	*2.46*	3.12	0.16	3.00
[b]PY5	S_1	*12.94*	0.53	6.89	0.28	6.29	0.42	15.03	3.30	9.64	2.75	*0.43*	*10.19*	*3.22*	*0.40*	*9.73*	3.30	0.43	9.65
[b]PY6	S_1	*16.51*	0.66	8.14	0.60	12.69	0.48	13.67	6.57	9.94	6.54	*0.45*	*9.96*	*7.76*	*0.37*	*8.75*	7.27	0.46	9.24
[b]PY7	S_1	*15.91*	0.68	8.66	0.58	12.60	0.49	13.56	6.80	9.11	6.74	*0.47*	*9.18*	*7.94*	*0.39*	*7.97*	7.49	0.48	8.42
[b]PY8	S_1	*19.32*	0.78	9.89	0.61	13.13	0.57	13.33	7.52	11.81	7.81	*0.52*	*11.52*	*9.27*	*0.43*	*10.05*	8.33	0.55	10.99

[a] ϵ_1: Lower Cambrian; S_1: Lower Silurian.
[b] The data in italic for PY samples are adopted from Tian et al. (2013).
[c] The C value here is the same asC_{BET}^{ext} (See details in text).

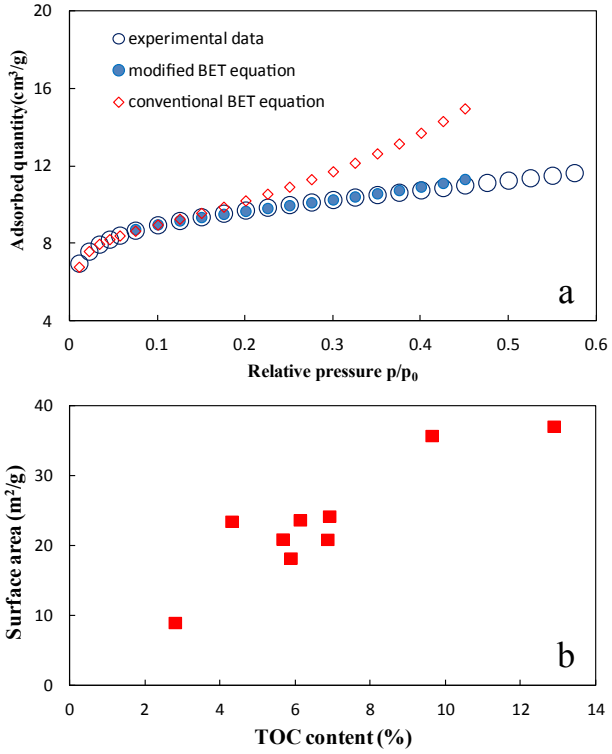

Figure 10. A comparison between the classic and modified BET equation (a, sample HY2) and the relationship between the TOC content and the total surface area calculated by classic BET equation (b).

The micropore volumes calculated by DR equation, modified BET equation and t-plot methods are also listed in Table 2. Figure 13 presents an example of how the micropore volumes are determined by the t-plot methods based on various models. While the micropore volume (V_{mic}) calculated by DR equation ranges from 0.36 cm^3/100 g to 1.53 cm^3/100 g, the V_{mic} values are in the range of 0.28–1.14 cm^3/100 g by modified BET equation, 0.27–1.14 cm^3/100 g by C-value based model (Lecloux and Pirard model, 1979), 0.25–1.59 cm^3/100 g by Harkins–Jura model (de Boer et al., 1966) and 0.20–1.02 cm^3/100 g by Carbon Black model (Magee, 1995). It is clear to see that the DR equation always yield the largest value among the micropore volumes. This is because that the DR equation is best used for purely microporous materials and could overestimate the micropore volume of a material when there are meso- and macro-pores and the extent of overestimation depends on the surface area of meso- and macro-pores, i.e., non-micropore area, in the materials (Remy and Poncelet, 1995; Schneider, 1995; Šolcová et al., 2009). The reason for the overestimation is that some molecules still can be adsorbed on the surface of meso- and macropores even in the application range of DR equation and these molecules are mistakenly accounted as the molecules that are filling micropores and therefore, the overestimation of micropore volume by DR equation is theoretically the product of the non-micropore surface area and the monomolecular thickness of N_2 at 77 K (Remy and Poncelet, 1995). As illustrated in Figure 14a, the overestimation of micropore volume, obtained by the difference between the micropore volumes calculated by DR equation and modified BET equation, is linearly related to the non-micropore surface area. The linear regression applied to our samples gives a slope of 0.0322 and an intercept near zero, with a correlation coefficient of 0.9841. The value of the slope is quite close to the value of 0.354 nm, the theoretical thickness of monomolecular N_2 at 77 K

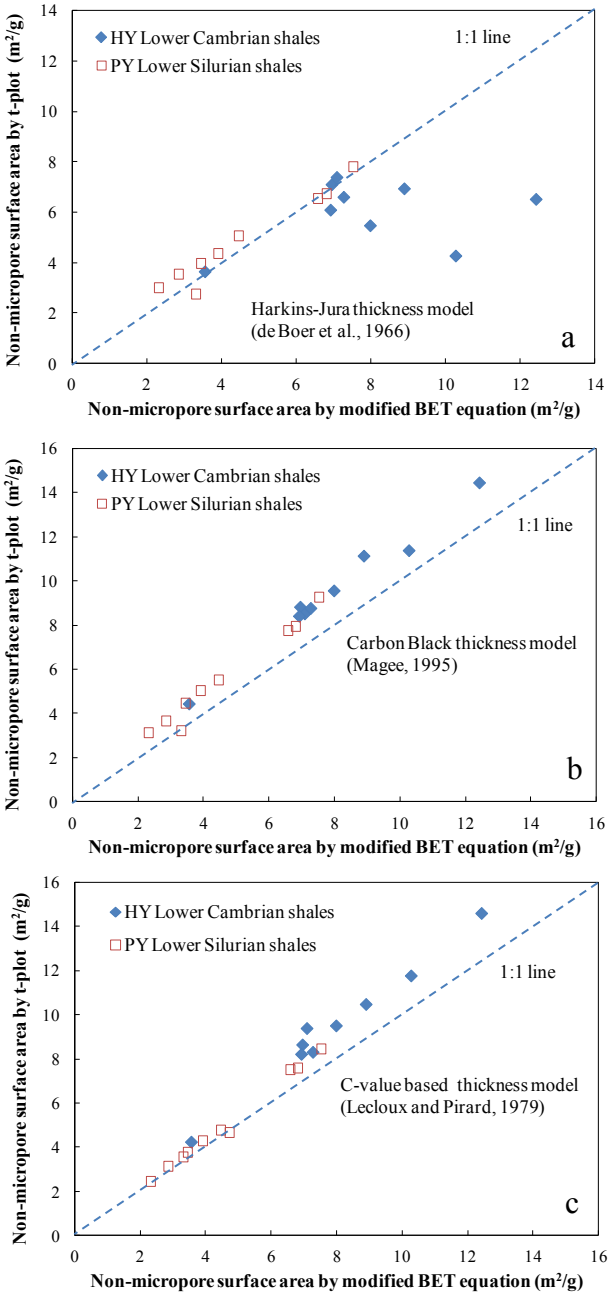

Figure 11. Plots showing the correlations of non-micropore surface areas calculated by the modified BET equation and various t-plot models. The non-micropore surface area here includes mainly the surface area of meso- and macro-pores (see details in Section 3.5 and 3.6). The Lower Silurian shale data (PY samples) were included to increase the size of dataset and fully evaluate the t-plot models used in this study.

(Sing et al., 1985). Due to our sample nature and dataset, the maximum non-micropore surface area is limited to about 13 m^2/g. However, when our data are plotted together with the results of Remy and Poncelet (1995) on zeolite materials, there is still a linear relationship with an intercept of near zero and a slope of 0.0362 (Fig. 11b), indicating that the overestimation of micropore volume by DR equation is applicable to shales with non-micropore surface area larger than our samples.

Figure 15 compares the micropore volumes calculated by BET equation and various t-plot models and reveals that the Harkins–Jura model predicts similar results as the BET equation when

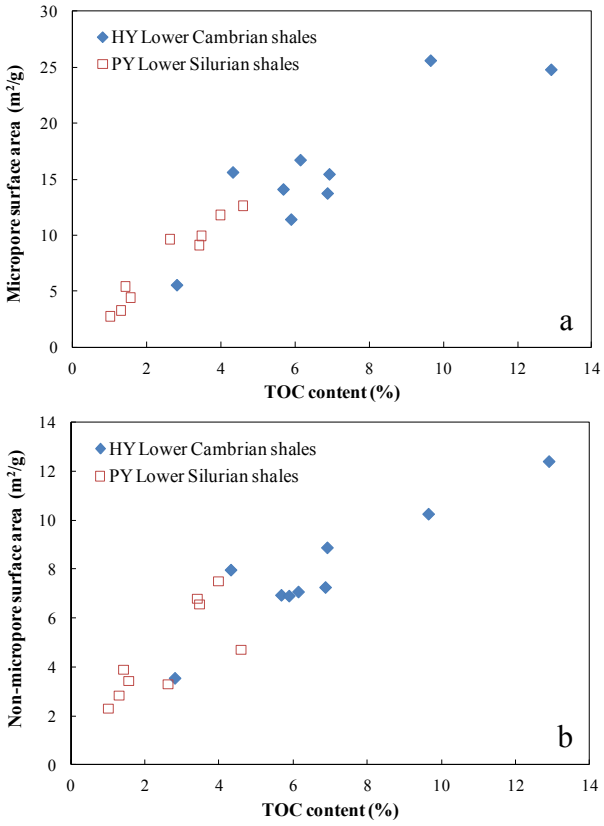

Figure 12. Plots showing the relationships between TOC content and micropore surface area (a) and non-micropore surface area (b). The non-micropore surface area was determined by modified BET equation and the micropore surface area was obtained by the difference between the total BET surface area and the non-micropore surface area. The Lower Silurian shale data (PY samples) were included to increase the size of dataset and fully evaluate these relationships.

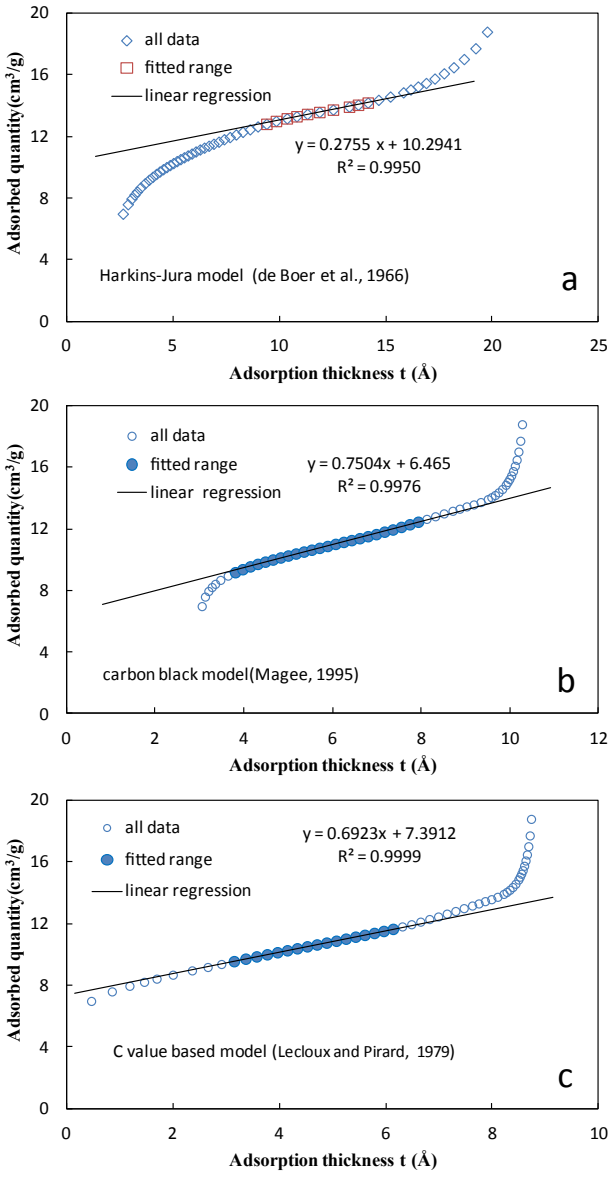

Figure 13. Plots showing the micropore volumes determined by t-plot method using various models (sample HY2). Note that the linearity in Harkins–Jura model is only observed in greater thickness values that are beyond the expected thickness range (e.g., 0.35 nm–1.0 nm) as originally suggested by de Boer et al. (1966), indicating this thickness model may not be applicable to the shale samples though it also gives linear range.

the micropore volume is less than 0.8 cm^3/100 g, but it yields larger values than the modified BET equation at increased micropore volumes (Fig. 15a). The micropore volumes estimated by Carbon Black model are generally lower than those determined by modified BET model, though they are linearly related (Fig. 15b). It is worthy to note that the C-valued based t-plot model predicts almost the same results as the modified BET equation in the whole range of micropores volumes covered by our samples (Fig. 15c), and this consistence between the two different methods indicates that the modified BET equation is a simple and useful method to evaluate the micropore volumes in shales. In addition, we also compares the micropore volumes by modified BET equation based on N_2 adsorption with those by DR equation applied to CO_2 adsorption (Fig. 15d). Generally the micropore volumes based on CO_2 adsorption are greater than the N_2 micropore volumes and this is caused by the fact that the N_2 adsorption at 77 K is kinetically restricted to fully fill the pores narrower than 0.7 nm due to the low temperature (Carrasco-Marín et al., 1996) and indicates that there are some narrow pores of less than 0.7 nm in our shales. Rexer et al. (2013) even reported shales samples from Denmark whose micropores are dominated by narrow pores of less than 0.7 nm.

4.6. BJH pore size distributions (PSDs)

The pore size distributions of the lower Cambrian shales calculated by BJH model are presented and compared with those of Lower Silurian shales (Tian et al., 2013) in Figure 16. The plot of *dV/d(logW) versus W* clearly reveals quite different PSDs for the two different sample groups, and basically there are more finer mesopores (e.g., 2–10 nm) in the Lower Cambrian shales (Fig. 16a, b). This observation is consistent with the geological fact that the Lower Cambrian shale underwent more severe compaction than the Lower Silurian shales, and partly explains why the porosity of organic matters in the Lower Cambrian shales is smaller than that in the Lower Silurian shales. It is also interesting to note that more fine mesopores can be observed in both group samples with increasing TOC content, implying that the fine mesopores are more easily developed in organic matter grains than in mineral matrix in the samples analyzed. For the distributions of specific surface area with respect to pore size, both the Lower Cambrian and Lower shales show similar shapes, and their surface areas are predominantly contributed by the pores smaller than 10 nm in width

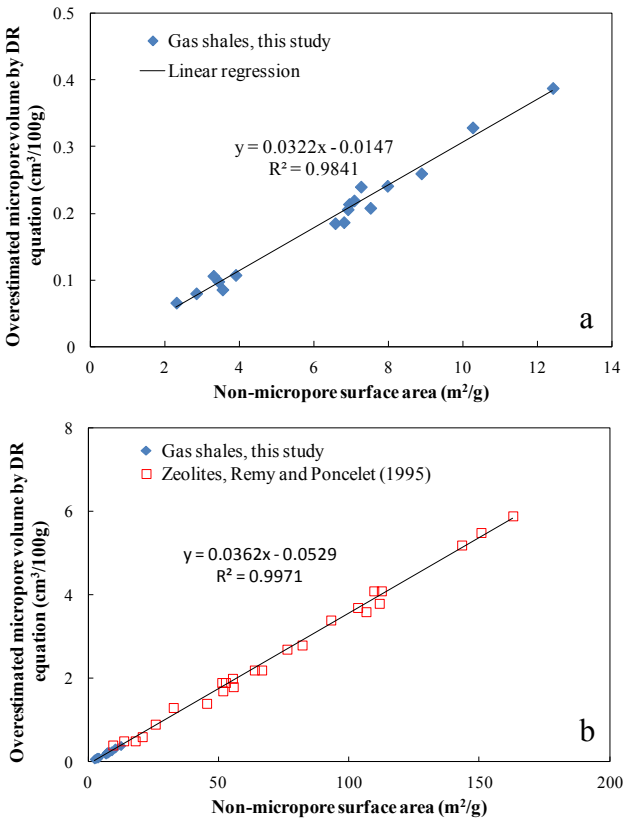

Figure 14. Plots showing the relationship between the overestimation of micropore volume by DR equation and the non-micropore surface area calculated by the modified BET equation for our shale samples (a) and for both shale and zeolite samples (b).

(Fig. 16c, d), which is consistent with the results for many gas shales in North American basins (Chalmers and Bustin, 2007, 2008; Ross and Bustin, 2009).

5. Conclusions

(1) The Lower Cambrian shales in Qiannan Depression of Southern Guizhou Province contain high TOCs ranging from 2.81% to 12.90%, thermally overmatured with equivalent vitrinite reflectance values in the range of 2.92–3.25%, and high clay contents ranging from 32.4% to 53.2%. The total porosity ranges from 2.46% to 4.13%, and total surface area varies from 9.08 to 37.19 m^2/g, both of which is positively related with TOC contents.

(2) FE-SEM observations reveal that both organic and inorganic pores are developed in the Lower Cambrian shales, and that not all grains of organic matters have the same porosity. Based on the plot of TOC *vs* total porosity, the average porosity of organic matters for the Lower Cambrian shales is estimated about 10%, far lower than the values for the Lower Silurian shales in and around Sichuan Basin and other shales in North America, which indicates either the pores in organic matters have been severely compacted or destroyed probably due to gas expulsion or they are not generated as abundantly as in other shales.

(3) Our study reveals that the modified BET equation applied to N_2 adsorption can be used conveniently to determine the micropore volumes/surface area and non-micropore surface areas for micropore-rich shales whereas the DR equation usually overestimates micropore volumes. The validity of modified BET equation to obtain micropore volume is also confirmed by the results obtained by another independent method, i.e. the t-plot method of Lecloux and Pirard (1979)

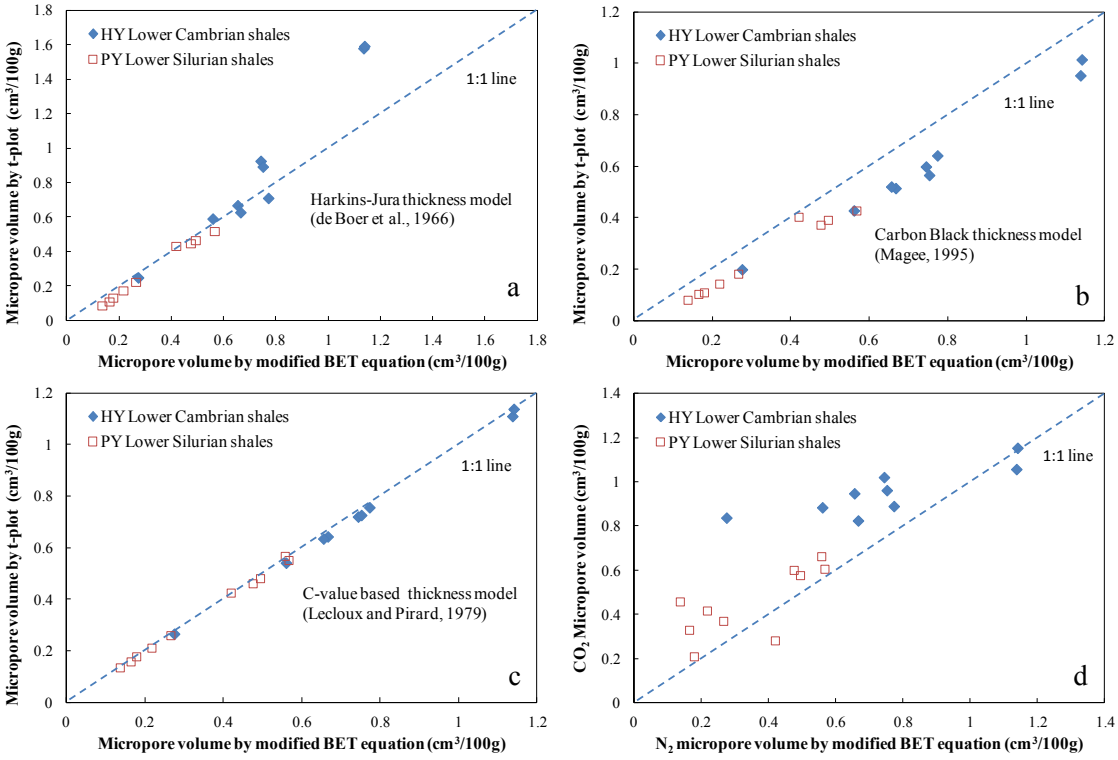

Figure 15. Plots showing the correlations of micropore volume calculated by the modified BET equation and various t-plot models (see details in Section 3.6). The Lower Silurian shale data (PY samples) were included to increase the size of dataset and fully evaluate these relationships.

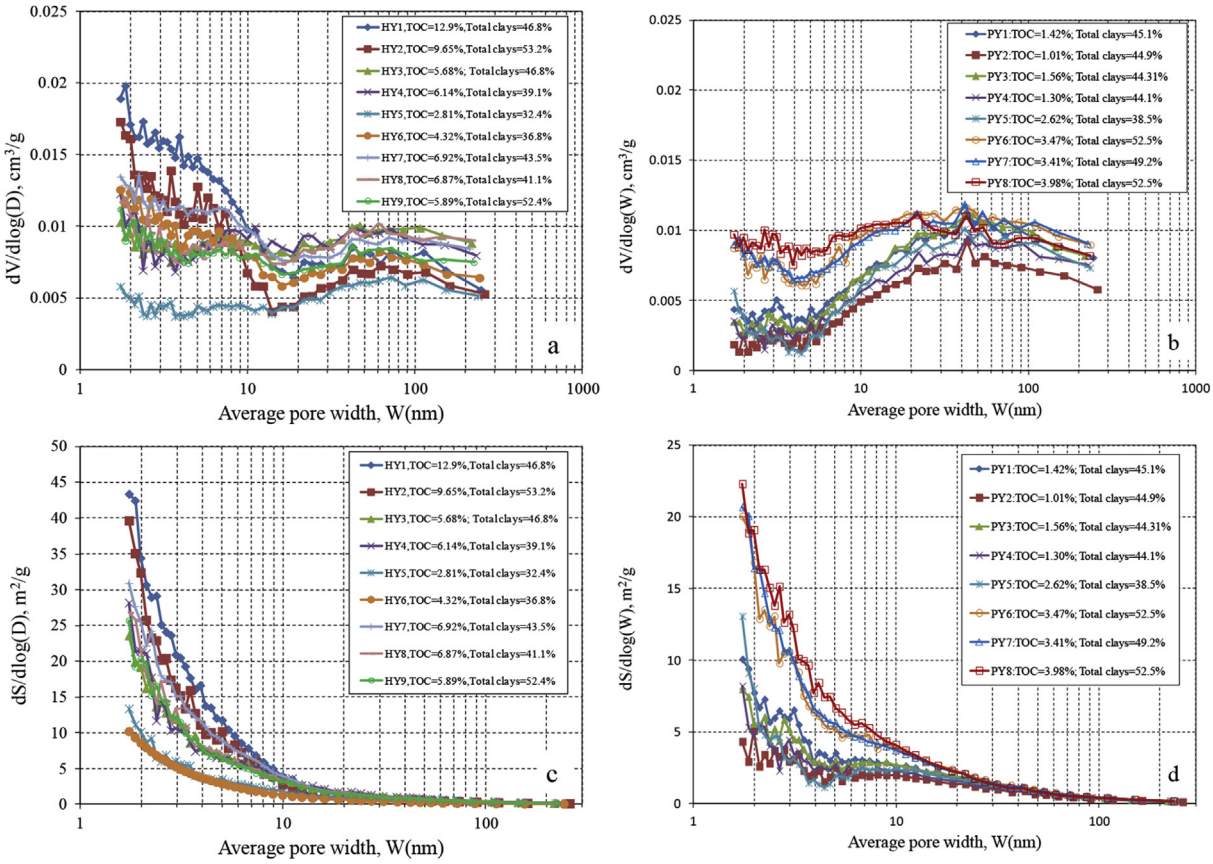

Figure 16. Plots showing the pore volume (a, b) and surface area (c, d) distributions with pore size derived from the N_2 adsorption branch of isotherms using BJH model. The Lower Silurian shales (PY samples) are adopted from Tian et al. (2013).

that correlates the adsorption thickness of nitrogen with the specific C values obtained in the modified BET equation.

Acknowledgments

This study was jointly supported by National key Basic Research Program of China (973 Program: 2012CB214705) and the Tukuangchi Talent Foundation (GIGRC-10-02). Special thanks to Drs Kuila, Marczewski and Prof. Hodson for their instructions on the t-plot method. Hui Tian is also grateful to the Youth Innovation Promotion Association, CAS for financial support. Associate Editor Jan de Jager and two anonymous reviewers are thanked for their instructive comments and suggestions that significantly help clarify this manuscript. This is contribution No. IS-2026 from GIGCAS.

References

Barrett, E.P., Joyner, L.G., Halenda, P.P., 1951. The determination of pore volume and area distribution in porous substances. I. Computations from nitrogen isotherms. J. Am. Chem. Soc. 73, 373–380.

Bernard, S., Wirth, R., Schreiber, A., Schulz, H.M., Horsfield, B., 2012. Formation of nanoporous pyrobitumen residues during maturation of the Barnett Shale (Fort Worth Basin). Int. J. Coal Geol. 103, 3–11.

Bruner, K.R., Smosna, R., 2011. A Comparative Study of the Mississippian Barnett Shale. Fort Worth Basin, and Devonian Marcellus Shale, Appalachian Basin. DOE/NETL-2011/1478.

Carrasco-Marín, F., Alvarez-Merino, M.A., Moreno-Castilla, C., 1996. Microporous activated carbons from a bituminous coal. Fuel 75, 966–970.

Chalmers, G.R., Bustin, R.M., Power, I.M., 2012a. Characterization of gas shale pore systems by porosimetry, pycnometry, surface area, and field emission scanning electron microscopy/transmission electron microscopy image analyses: examples from the Barnett, Woodford, Haynesville, Marcellus, and Doig units. AAPG Bull. 96, 1099–1119.

Chalmers, G.R., Bustin, R.M., Powers, I., 2009. A pore by any other name would be as small: the importance of meso- and microporosity in shale gas capacity. AAPG Search Discov. Article 90090, 1 p http://www.searchanddiscovery.com/abstracts/html/2009/annual/abstracts/chalmers.htm (accessed 14.03.14.).

Chalmers, G.R.L., Bustin, R.M., 2007. The organic matter distribution and methane capacity of the Lower Cretaceous strata of Northeastern British Columbia, Canada. Int. J. Coal Geol. 70, 223–339.

Chalmers, G.R.L., Bustin, R.M., 2008. Lower Cretaceous gas shales in northeastern British Columbia, Part I: geological controls on methane sorption capacity. Bull. Can. Pet. Geol. 56, 1–21.

Chalmers, G.R.L., Ross, D.J.K., Bustin, R.M., 2012b. Geological controls on matrix permeability of Devonian Gas Shales in the Horn River and Liard basins, northeastern British Columbia, Canada. Int. J. Coal Geol. 103, 120–131.

Chen, S., Zhu, Y., Wang, H., Liu, H., Wei, W., Fang, J., 2011. Shale gas reservoir characterization: a typical case in the southern Sichuan Basin of China. Energy 36, 6609–6616.

Clarkson, C.R., Freeman, M., He, L., Agamalian, M., Melnichenko, Y.B., Mastalerz, M., Bustin, R.M., Radlinski, A.P., Blach, T.P., 2012a. Characterization of tight gas reservoir pore structure using USANS/SANS and gas adsorption analysis. Fuel 95, 371–385.

Clarkson, C.R., Jensen, J.L., Pedersen, P.K., Freeman, M., 2012b. Innovative methods for flow-unit and pore-structure analyses in a tight siltstone and shale gas reservoir. Am. Assoc. Pet. Geol. Bull. 96, 355–374.

Clarkson, C.R., Wood, J.M., Burgis, S.E., Aquino, S.D., Freeman, M., 2012c. Nanopore-structure analysis and permeability predictions for a tight gas siltstone reservoir by use of low pressure adsorption and mercury intrusion techniques. SPE Reserv. Eval. Eng. 648–661.

Coasne, B., Gubbins, K.E., Pellenq, R.J.-M., 2004. A Grand Canonical Monte Carlo study of adsorption and capillary phenomena in nanopores of various morphologies and topologies: testing the BET and BJH characterization methods. Part. Part. Syst. Charact. 21, 149–160.

Curtis, J.B., 2002. Fractured shale-gas systems. AAPG Bull. 86, 1921–1938.

Curtis, M.E., Cardott, B.J., Sondergeld, C.H., Rai, C.S., 2012a. Development of organic porosity in the Woodford Shale with increasing thermal maturity. Int. J. Coal Geol. 103, 26–31.

Curtis, M.E., Ambrose, R.J., Sondergeld, C.H., Rai, C.S., 2012b. Microstructural investigation of gas shales in two and three dimensions using nanometer-scale resolution imaging. AAPG Bull. 96, 665–677.

de Boer, J.H., Lippens, B.C., Linsen, B.G., Broekhoff, J.C.P., van den Heuvel, A., Osinga, ThJ., 1966. The t-curve of multimolecular N_2-adsorption. J. Colloid Interface Sci. 21, 405–414.
Furmann, A., Mastalerz, M., Schimmelmann, A., Pedersen, P.K., Bish, D., 2014. Relationships between porosity, organic matter, and mineral matter in mature organic-rich marine mudstones of the Belle Fourche and Second White Specks formations in Alberta, Canada. Mar. Pet. Geol. 54, 65–81.
Groen, J.C., Peffer, L.A.A., Pérez-Ramírez, J., 2003. Pore size determination in modified micro- and mesoporous materials. Pitfalls and limitations in gas adsorption data analysis. Microporous Mesoporous Mater. 60, 1–17.
Han, S., Zhang, J., Li, Y., Horsfield, B., Tang, X., Jiang, W., Chen, Q., 2013. Evaluation of Lower Cambrian shale in northern Guizhou province, South China: implications for shale gas potential. Energy & Fuels 27, 2933–2941.
Hao, F., Zou, H., 2013. Cause of shale gas geochemical anomalies and mechanisms for gas enrichment and depletion in high-maturity shales. Mar. Pet. Geol. 44, 1–12.
He, X., Yao, G., Cai, C., Shen, A., Wu, J., Huang, L., Chen, Z., 2012. Aromatic hydrocarbons distribution in oil seepages from the southern Guizhou Depression, SW China: geochemical characteristics and geological implications. Geochimica 41, 442–451 (In Chinese with English abstract).
He, X.Y., Cai, C.F., Yao, G.S., Xiong, X.H., Shen, A.J., Xiang, L., Wu, J.W., 2013. Origins of oil seepages in the Southern Guizhou Depression, SW China: evidence from carbon isotopes, sulfur isotopes and biomarkers. Acta Petrol. Sin. 29, 1059–1072 (In Chinese with English abstract).
Hill, R.J., Zhang, E., Katz, B.J., Tang, Y., 2007. Modeling of gas generation from the Barnett shale, Fort Worth Basin, Texas. AAPG Bull. 91, 501–521.
Hodson, M.E., 1999. Micropore surface area variation with grain size in unweathered alkali feldspars: implications for surface roughness and dissolution studies. Geochim. Cosmochim. Acta 62, 3429–3435.
Hou, D., Bao, S., Mao, X., Chen, X., Ma, N., Zhang, X., Yang, G., Sun, C., 2012. Discussions on the key issues of resource potential evaluation for shale gas. J. Earth Sci. Environ. 34, 7–16 (in Chinese with English abstract).
Jarvie, D.M., Hill, R.J., Ruble, T.E., Pollastro, R.M., 2007. Unconventional shale-gas systems: the Mississippian Barnett Shale of north-central Texas as one model for thermogenic shale-gas assessment. AAPG Bull. 91, 475–499.
Kuila, U., Prasad, M., 2013. Specific surface area and pore-size distribution in clays and shales. Geophys. Prospect. 61, 341–362.
Lecloux, A., Pirard, J.P., 1979. The importance of standard isotherms in the analysis of adsorption isotherms for determining the porous texture of solids. J. Colloid Interface Sci. 70, 265–281.
Long, P., Zhang, J., Jiang, W., Nie, H., Tang, X., Han, S., Xing, Y., 2012. Analysis on pores forming features and its influence factors of reservoir well Yuye-1. J. Central South Univ. Sci. Technol. 43, 3954–3963.
Loucks, R.G., Reed, R.M., Ruppel, S.C., Jarvie, D.M., 2009. Morphology, genesis, and distribution of nanometer-scale pores in siliceous mudstones of the Mississippian Barnett Shale. J. Sediment. Res. 79, 848–861.
Loucks, R.G., Reed, R.M., Ruppel, S.C., Hammes, U., 2012. Spectrum of pore types and networks in mudrocks and a descriptive classification for matrix-related mudrock pores. AAPG Bull. 96, 1071–1098.
Magee, R.W., 1995. Evaluation of the external surface area of carbon black by nitrogen adsorption. Rubber Chem. Technol. 68, 590–600.
Mahlstedt, N., Horsfield, B., 2012. Metagenetic methane generation in gas shales I. Screening protocols using immature samples. Mar. Pet. Geol. 31, 27–42.
Marcilla, A., Gómez-Siurana, A., Muñoz, M.J., Valdés, F.J., 2009. Comments on the methods of characterization of textural properties of solids from gas adsorption data. Adsorpt. Sci. Technol. 27, 69–84.
Mastalerz, M., He, L., Melnichenko, Y.B., Rupp, J.A., 2012. Porosity of coal and shale: insights from gas adsorption and SANS/USANS techniques. Energy & Fuels 26, 5109–5120.
Mastalerz, M., Schimmelmann, A., Drobniak, A., Chen, Y., 2013. Porosity of Devonian and Mississippian New Albany Shale across a maturation gradient: insights from organic petrology, gas adsorption, and mercury intrusion. AAPG Bull. 97, 1621–1643.
Mei, M., Zhang, H., Meng, X., Chen, Y., 2006. Sequence stratigraphic division and framework of the Lower Cambrian in the Upper Yangtze region. Geol. China 33, 1292–1304 (in Chinese with English abstract).
Milliken, K.L., Rudnicki, M., Awwiller, D.N., Zhang, T., 2013. Organic matter–hosted pore system, Marcellus formation (Devonian), Pennsylvania. AAPG Bull. 97, 177–200.
Modica, C.J., Lapierre, S.G., 2012. Estimation of kerogen porosity in source rocks as a function of thermal transformation: example from the Mowry Shale in the Powder River Basin of Wyoming. AAPG Bull. 96, 87–108.
Montgomery, S.L., Jarvie, D.M., Bowker, K.A., Pollastro, R.M., 2005. Mississippian Barnett Shale, Fort Worth Basin, north-central Texas: gas-shale play with multitrillion cubic foot potential. AAPG Bull. 89, 155–175.
Mosher, K., He, J., Liu, Y., Rupp, E., Wilcox, J., 2013. Molecular simulation of methane adsorption in micro- and mesoporous carbons with applications to coal and gas shale systems. Int. J. Coal Geol. 109–110, 36–44.
Nelson, P.H., 2009. Pore throat sizes in sandstones, tight sandstones, and shales. AAPG Bull. 93, 1–13.
Passey, Q.R., Bohacs, K.M., Esch, W.L., Klimentidis, R., Sinha, S., 2010. From oil-prone source rock to gas-producing shale reservoir – Geologic and petrophysical characterization of unconventional shale-gas reservoirs. In: International Oil and Gas Conference and Exhibition in China, 8-10 June, 2010, Beijing, China. http://dx.doi.org/10.2118/131350-MS.
Pepper, A.S., Dodd, T.A., 1995. Simple kinetic models of petroleum formation. Part II: oil-gas cracking. Mar. Pet. Geol. 12, 321–340.
Pollastro, R.M., 2007. Total petroleum system assessment of undiscovered resources in the giant Barnett Shale continuous (unconventional) gas accumulation, Fort Worth Basin, Texas. AAPG Bull. 91, 551–578.
Ratcliffe, K., Wright, M., 2012. Unconventional methods for unconventional plays: using elemental data to understand shale resource plays. PESA News Resour. 2012, 55–60.
Remy, M.J., Poncelet, G., 1995. A new approach to the determination of the external surface and micropore volume of zeolites from the nitrogen adsorption isotherm at 77 K. J. Phys. Chem. 99, 773–779.
Rexer, T.F.T., Benham, M.J., Aplin, A.C., Thomas, K.M., 2013. Methane adsorption on shale under simulated geological temperature and pressure conditions. Energy & Fuels 27, 3099–3109.
Ross, D.J.K., Bustin, R.M., 2008. Characterizing the shale gas resource potential of Devonian-Mississippian strata in the Western Canada Sedimentary Basin: application of an integrated formation evaluation. AAPG Bull. 92, 87–125.
Ross, D.J.K., Bustin, R.M., 2009. The importance of shale composition and pore structure upon gas storage potential of shale gas reservoirs. Mar. Pet. Geol. 26, 916–927.
Rouquerol, J., Llewellyn, P., Rouquerol, F., 2007. Is the BET equation applicable to microporous adsorbents? Stud. Surf. Sci. Catal. 160, 49–56.
Scherdel, C., Reichenauer, G., Wiener, M., 2010. Relationship between pore volumes and surface areas derived from the evaluation of N_2-sorption data by DR-, BET- and t-plot. Microporous Mesoporous Mater. 132, 572–575.
Schmitt, M., Fernandes, C.P., da Cunha Neto, J.A.B., Wolf, F.B., dos Santos, V.S.S., 2013. Characterization of pore systems in seal rocks using nitrogen gas adsorption combined with mercury injection capillary pressure techniques. Mar. Pet. Geol. 39, 138–149.
Schneider, P., 1995. Adsorption isotherms of microporous-mesoporous solids revisited. Appl. Catal. A: General 129, 157–165.
Schoenherr, J., Littke, R., Urai, J.L., Kukla, P.A., Rawahi, Z., 2007. Polyphase thermal evolution in the Infra-Cambrian Ara group (South Oman salt basin) as deduced by maturity of solid reservoir bitumen. Org. Geochem. 38, 1293–1318.
Sigal, R.F., 2012. A Note on the Intrinsic Porosity of Organic Material in Shale Gas Reservoir Rocks. http://shale.ou.edu/Home/Publication.
Sing, K.S., Everett, D.H., Haul, R.A.W., Moscou, L., Pierotti, R.A., Rouquerol, J., Siemieniewsha, T., 1985. Reporting physisorption data for gas/solid systems with special reference to the determination of surface area and porosity. Pure Appl. Chem. 57, 603–619.
Šolcová, O., Matějová, L., Hudec, P., Schneider, P., 2009. Modified BET equation for determination of micropore pore-volume and mesopore surface area in microporous-mesoporous solids. In: Kaskel, S., Llewellyn, P., Rodriguze-Reinoso, F., Seaton, N.A. (Eds.), Characterisation of Porous Solids VIII: Proceedings of the 8th International Symposium on the Characterisation of Porous Solids. The Royal Society of Chemistry, Cambridge, pp. 218–224.
Sousa-Aguiar, E.F., Liebsch, A., Chaves, B.C., Costa, A.F., 1998. Influence of the external surface area of small crystallite zeolites on the micropore volume determination. Microporous Mesoporous Mater. 25, 185–192.
Stach, E., Mackowsky, M.-T., Teichmüller, M., Taylor, G.H., Chandra, D., Teichmüller, R., 1982. Stach's Textbook of Coal Petrology. Gebrüder Borntraeger, Stuttgart.
Strąpoć, D., Mastalerz, M., Schimmelmann, A., Drobniak, A., Hasenmueller, N.R., 2010. Geochemical constraints on the origin and volume of gas in the New Albany Shale (Devonian–Mississippian), eastern Illinois Basin. AAPG Bull. 94, 1713–1740.
Sun, W., Liu, S., Ran, B., Wang, S., Ye, Y., Luo, C., Tian, M., 2012. General situation and prospect evaluation of the shale gas in Niutitang Formation of Sichuan Basin and its surrounding areas. J. Chengdu Univ. Technol. Sci. Technol. Ed. 39, 170–175.
Tan, J., Horsfield, b., Fink, R., Krooss, B., Schulz, H.-M., Rybacki, E., Zhang, J., Boreham, C.J., van Graas, G., Tocher, B.A., 2014. Shale gas potential of the major marine shale formations in the Upper Yangtze Platform, South China, Part III: mineralogical, lithofacial, petrophysical, and rock mechanical properties. Energy & Fuels 28, 2322–2342.
Taylor, H., Teichmüller, M., Davis, A., Diessel, C.F.K., Littke, R., Robert, P., 1998. Organic Petrology. Borntraeger, Berlin-Stuttgart.
Tian, H., Pan, L., Xiao, X., Wilkins, R.W.T., Meng, Z., Huang, B., 2013. A preliminary study on the pore characterization of Lower Silurian black shales in the Chuandong Thrust Fold Belt, southwestern China using low pressure N_2 adsorption and FE-SEM methods. Mar. Pet. Geol. 48, 8–19.
Wang, F., Guan, J., Feng, W., Bao, L., 2013. Evolution of overmature marine shale porosity and implication to the free gas volume. Pet. Explor. Dev. 40, 819–824.
Wang, L., Zou, C., Zheng, P., Chen, S., Zhang, Q., Xu, B., Li, H., 2009. Geochemical evidence of shale gas existed in the Lower Paleozoic Sichuan basin. Nat. Gas. Ind. 29, 59–62.

Wang, Y., Zhu, Y., Chen, S., Li, W., 2014. Characteristics of the Nanoscale pore structure in Northwestern Hunan shale Gas reservoirs using field emission scanning electron microscopy, high-pressure mercury intrusion, and Gas adsorption. Energy & Fuels 28, 945–955.

Wu, G., Wang, W., Chi, H., 2012. Basin evolution and later reformation of marine sediments in southern Guizhou depression and neighboring areas. J. Palaeogeogr. 14, 507–521 (in Chinese with English abstract).

Xia, X., Chen, J., Braun, R., Tang, Y., 2013. Isotopic reversals with respect to maturity trends due to mixing of primary and secondary products in source rocks. Chem. Geol. 339, 205–212.

Xu, Z., Yao, G., Guo, Q., Chen, Z., Dong, Y., Wang, P., Ma, L., 2010. Genetic interpretation about geotectonics and structural transfiguration of the Southern Guizhou Depression. Geotect. Metallog. 34, 20–31 (in Chinese with English abstract).

Zeng, H., 2012. The quantitative evaluation of inorganic pores in shales of Jiumenchong formation, Qiannan Depression. J. Oil Gas Technol. 35, 34–39 (in Chinese).

Zhang, T.W., Ellis, G.S., Rupple, S.C., Milliken, K., Yang, R., 2012. Effect of organic-matter type and thermal maturity on methane adsorption in shale-gas systems. Org. Geochem. 47, 120–131.

Zou, C., Dong, D., Wang, S., Li, J., Li, X., Wang, Y., Li, D., Cheng, K., 2010. Geological characteristics and resource potential of shale gas in China. Pet. Explor. Dev. 37, 641–653.